Physics of the Earth and Planetary Interiors 251 (2016) 24–35

Contents lists available at ScienceDirect

Physics of the Earth and Planetary Interiors

journal homepage: www.elsevier.com/locate/pepi

Crystal structure, equation of state, and elasticity of hydrous aluminosilicate phase, topaz-OH ($Al_2SiO_4(OH)_2$) at high pressures

Mainak Mookherjee [a,*], Jun Tsuchiya [b,c], Anant Hariharan [d]

[a] Earth, Ocean and Atmospheric Sciences, Florida State University, Tallahassee FL, 32306, USA
[b] Geodynamics Research Center, Ehime University, 2-5 Bunkyo-cho, Matsuyama, Ehime 790-8577, Japan
[c] Earth-Life Science Institute, Ehime Satellite, 2-5 Bunkyo-cho, Matsuyama, Ehime 790-8577, Japan
[d] Earth and Atmospheric Sciences, Cornell University, Ithaca, NY 14853, USA

ARTICLE INFO

Article history:
Received 6 April 2015
Received in revised form 11 August 2015
Accepted 18 November 2015
Available online 2 December 2015

Keywords:
Elasticity
High pressure
Topaz
Subduction
Sediments

ABSTRACT

We examined the equation of state and high-pressure elasticity of the hydrous aluminosilicate mineral topaz-OH ($Al_2SiO_4(OH)_2$) using first principles simulation. Topaz-OH is a hydrous phase in the Al_2O_3–SiO_2–H_2O (ASH) ternary system, which is relevant for the mineral phase relations in the hydrated sedimentary layer of subducting slabs. Based on recent neutron diffraction experiments, it is known that the protons in the topaz-OH exhibit positional disorder with half occupancy over two distinct crystallographic sites. In order to adequately depict the proton environment in the topaz-OH, we examined five crystal structure models with distinct configuration for the protons in topaz-OH. Upon full geometry optimization we find two distinct space group, an orthorhombic *P*bnm and a monoclinic $P2_1/c$ for topaz-OH. The topaz-OH with the monoclinic $P2_1/c$ space group has a lower energy compared to the orthorhombic *P*bmn space group symmetry. The pressure–volume results for the monoclinic topaz-OH is well represented by a third order Birch–Murnaghan formulation, with V_0^{mon} = 348.63 (±0.04) Å^3, K_0^{mon} = 164.7 (±0.04) GPa, and K_0^{mon} = 4.24 (±0.05). The pressure–volume results for the orthorhombic topaz-OH is well represented by a third order Birch–Murnaghan formulation, with V_0^{orth} = 352.47 (±0.04) Å^3, K_0^{orth} = 166.4 (±0.06) GPa, and K_0^{orth} = 4.03 (±0.04). While the bulk moduli are very similar for both the monoclinic and orthorhombic topaz-OH, the shear elastic constants and the shear moduli are very sensitive to the position of the proton, orientation of the O–H dipole, and the space group symmetry. The S-wave anisotropy for the orthorhombic and monoclinic topaz-OH are also quite distinct.

In the hydrated sedimentary layer of subducting slabs, transformation of a mineral assemblage consisting of coesite (SiO_2) and diaspore (AlOOH) to topaz-OH ($Al_2SiO_4(OH)_2$) is likely to be accompanied by an increase in density, compressional velocity, and shear wave velocity. However, further studies of physical properties and lattice preferred orientation of several key hydrous aluminosilicates needs to be prioritized for gaining better insight into the transport of water via subduction of sediments.

1. Introduction

Subduction zones are major tectonic sites where sediments, oceanic crust, and mantle lithosphere descend into the Earth's interior. The oceanic crust is often hydrated owing to shallow water circulations along the faults associated with the spreading centers (Stern, 2002). In the process of descending into the Earth's interior, the cold oceanic lithosphere bends and generates bending related faults, which leads to hydration of the underlying mantle (Ranero et al., 2003).

There are distinctive differences in the major element chemistry of the sediments, oceanic crust, and the mantle (Hacker, 2008). The alumina (Al_2O_3) and silica (SiO_2) contents of the sediments and the oceanic crusts are greater compared to mafic mantle rocks. For instance, typical pelite may contain ~63.4 wt% SiO_2 and 18.0 wt% Al_2O_3 (Miller, 1985) and typical mid ocean ridge basalt (MORB) may contain ~50.6 wt% SiO_2 and 15.7 wt%Al_2O_3 (Hacker, 2008 and references there in). This is in contrast with an altered peridotite which may contain ~47.9 wt% SiO_2 and 2.7 wt% Al_2O_3 (Hacker, 2008 and references there in). Owing to the abundance of alumina and silica, hydrated sediment layers could be modeled in a simplified Al_2O_3–SiO_2–H_2O (ASH) ternary system (Peacock, 1990; Schreyer, 1995). Based on thermodynamic constraints on mineral assemblages and mineral transformations, it was

* Corresponding author.
E-mail address: mmookherjee@fsu.edu (M. Mookherjee).

http://dx.doi.org/10.1016/j.pepi.2015.11.006
0031-9201/

Table 1
Crystal structure models for topaz-OH used in this study and the details of the crystal structure after full geometry optimization.

	Initial	Converged symmetry, lattice parameters, energy						
	Sp. group	Sp.group	a [Å]	b [Å]	c [Å]	β [^{0}]	V [Å^3]	E [eV]
Model #1	*P*bnm	*P*bnm	4.59449	8.93063	8.42067	90.000	345.51	−323.19045084
Model #2	*P*bnm	*P*bnm	4.59449	8.93063	8.42067	90.000	345.51	−323.19045084
Model #3	$P2_1/c$	$P2_1/c$	4.71992	8.87322	8.24982	90.124	345.51	−323.57385418
Model #4	$P2_1/m$	*P*bnm	4.59449	8.93063	8.42067	90.000	345.51	−323.19045084
Model #5	*P*-1	$P2_1/c$	4.71992	8.87322	8.24982	90.124	345.51	−323.57385418
	Hydrogen positions							
	Initial						Converged	
	x_{H1}	y_{H1}	z_{H1}	x_{H2}	y_{H2}	z_{H2}	x_{H1}	y_{H1}	z_{H1}	x_{H2}	y_{H2}	z_{H2}
Model #1	0.4620	0.1822	0.1190				0.4398	0.2257	0.1425			
Model #2				0.5160	0.2740	0.1772				0.4399	0.2258	0.1426
Model #3	0.4620	0.1822	0.1190	0.0160	0.2260	0.8228	0.4258	0.1617	0.0782	0.0427	0.2242	0.8082
Model #4	0.9620	0.3178	0.8810	0.5160	0.2740	0.1772	0.4398	0.2257	0.1425			
Model #5	0.4620	0.1822	0.1190	0.0160	0.2260	0.8228	0.4258	0.1618	0.0782	0.0428	0.2241	0.8082

predicted that for cold subduction zones with thermal gradients less than ~4 °C/km, layered hydrous silicate such as kaolinite ($Al_2Si_2O_5(OH)_4$) is likely to decompose to a mixture of diaspore (AlOOH), quartz (SiO_2), and water (H_2O) at 1.5 GPa and 200 °C (Peacock, 1990). The mixture of diaspore (AlOOH) and quartz (SiO_2) will eventually transform to kyanite (Al_2SiO_5) and water (H_2O) at <3.5 GPa and 400 °C (Peacock, 1990). However, later experimental studies on the ASH ternary system revealed that the hydrous aluminosilicate mineral phases such as phase pi ($Al_3Si_2O_7(OH)_3$) and topaz-OH ($Al_2SiO_4(OH)_2$) are likely to retain the water up to a pressures of around ~8 GPa (Wunder et al., 1993a,b; Schreyer, 1995). Further experimental studies on the hydrated sedimentary rocks revealed that topaz-OH is likely to be stable up to 12 GPa (Ono, 1998). Topaz-OH is likely to transform to a higher pressures hydrous aluminosilicate mineral phase Egg ($AlSiO_3(OH)$) at pressures beyond 12 GPa (Ono, 1998, *and references therein*). The phase Egg has been reported within the inclusions of natural diamond (Wirth et al., 2007). This certainly indicates that sedimentary rocks are dragged into the deep Earth interior of the earth through the subducting slabs. Despite being an important mineral phase in transporting water into the Earth's interior, very little is known about the elasticity of hydrous aluminosilicates such as topaz-OH ($Al_2SiO_4(OH)_2$). Most of the high-pressure experiments on topaz have focused on constraining the equation of state of natural fluorine rich topaz samples (Komatsu et al., 2003; Gatta et al., 2006, 2014). Additional research on the crystal chemistry of topaz has been conducted to determine the location of protons within the crystal structure using vibrational spectroscopy (Bradbury and Williams, 2003; Watenphul and Wunder, 2010; Wunder et al., 1999), neutron diffraction (Northrup et al., 1994; Komatsu et al., 2008; Chen et al., 2005), and theoretical methods (Churakov and Wunder, 2004). A full elastic constant tensor of fluoride end-member topaz ($Al_2SiO_4F_2$) has been reported at ambient conditions (Haussühl, 1993). However, elasticity of topaz-OH remains unknown. In this study, using first principles simulations we present the first results of the full elastic constant tensor of topaz-OH ($Al_2SiO_4(OH)_2$) at high-pressures.

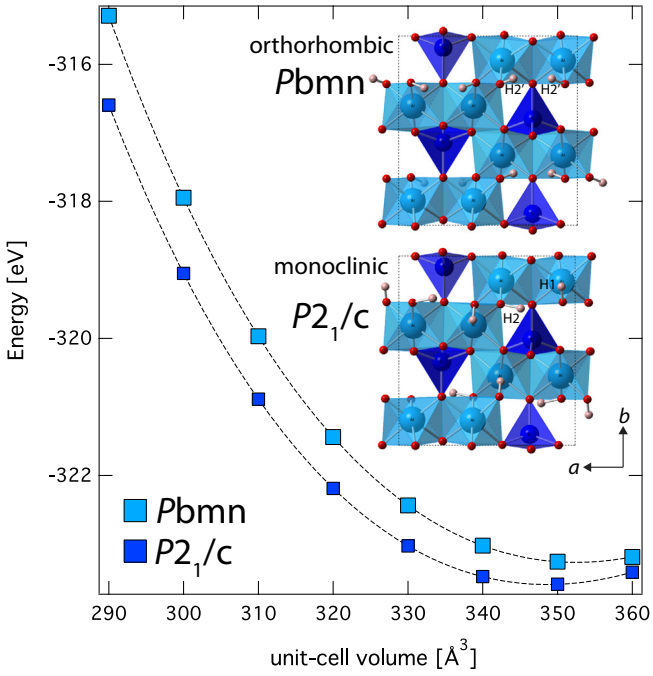

Fig. 1. Equation of state- plot of energy vs. unit-cell volume of topaz-OH, $Al_2SiO_4(OH)_2$. Dark blue symbols-monoclinic topaz-OH, light blue symbols- orthorhombic topaz-OH, and the dashed lines represent Birch–Murnaghan finite strain formulation (Birch, 1978; Chheda et al., 2014; Mookherjee and Tsuchiya, 2015a). Inset shows the crystal structure of topaz-OH (top) orthorhombic topaz-OH with *P*bnm spacegroup symmetry (bottom) monoclinic topaz-OH with $P2_1/c$ spacegroup symmetry. In both *P*bnm and $P2_1/c$ topaz-OH, the crystal structure consists of SiO_4 tetrahedral units and AlO_6 octahedral units. The main distinction between the *P*bmn and $P2_1/c$ lies in the hydrogen position. The monoclinic topaz-OH with $P2_1/c$ spacegroup has two distinct hydrogen position H1 and H2, whereas the orthorhombic topaz-OH with *P*bmn spacegroup symmetry has a single H2' hydrogen position (Table 1). The edge sharing AlO_6 octahedral units forms a crankshaft chain along the *c*-axis direction (Ribbe and Gibbs, 1971). The dark blue spheres represent silicon atoms, the light blue spheres represent aluminum atoms, the red spheres represent oxygen atoms, and the off-white spheres represent hydrogen atoms. (For interpretation of the references to colour in this figure legend, the reader is referred to the web version of this article.)

2. Method

2.1. First Principle Simulations

We used *first principles* simulation based on density functional theory calculations (Hohenberg and Kohn, 1964; Kohn and Sham, 1965) using with Vienna ab initio simulation package (VASP) (Kresse and Hafner, 1993; Kresse and Furthmüller, 1996a,b; Kresse and Joubert, 1999) to explore the crystal structure, equation of state, and elasticity at high pressure. We used generalized gradient approximation (GGA) (Perdew and Wang, 1986; Perdew et al., 1991; Perdew et al., 1996) for the exchange and correlation potentials. In addition, we used the highly accurate projector augmented wave method (PAW) as implemented in VASP (Kresse and Joubert, 1999). A dispersion correction to account for the van der Waals

interactions resulting from dynamical correlations between fluctuating charge distributions was added, as implemented in VASP (Grimme, 2006).

For the GGA calculations using VASP, we performed a series of convergence test by varying the energy cutoff and *k*-points. We found that an energy cut-off E_{cut} = 800 eV and a *k*-point mesh of 6 × 3 × 4 Monkhorst–Pack grid (Monkhorst and Pack, 1976) with 24 irreducible *k*-points is sufficient for describing the energetics (Supplementary Table 1). Full elastic constant tensor were determined by straining the lattice by 1%, the details of the methods are described in (Karki et al., 2001). Finite strain fits to the elasticity data, the computation of isotropic bulk (K), and shear (G) moduli were made using the finite strain formulations as in (Karki et al., 2001). Previous density functional theory based studies have been successful in predicting physical properties, particularly elasticity of hydrous minerals at conditions relevant to Earth's mantle (Chantel et al., 2012; Militzer et al., 2011; Mookherjee and Capitani, 2011; Mookherjee et al., 2015; Stackhouse et al., 2004; Tsuchiya et al., 2008; Tsuchiya, 2013a,b; Mookherjee and Tsuchiya, 2015b). We have calculated the single crystal azimuthal anisotropy for compressional (V_P) and shear (V_S) waves in topaz using the formulation for maximum polarization anisotropy (Mainprice, 1990).

2.2. Crystal structure model

The crystal structure of topaz ($Al_2SiO_4F_2$) consists of crankshaft chains of edge sharing AlO_6 octahedral units and corner sharing SiO_4 tetrahedral units (Pauling, 1928; Ribbe and Gibbs, 1971; Northrup et al., 1994; Gatta et al., 2006). The fluorine anion (F^-) could also be substituted with hydroxyl anion (OH^-) forming the hydrogen end member of topaz ($Al_2SiO_4(OH)_2$), referred as topaz-OH (Wunder et al., 1993a). The position of the hydrogen in topaz has been reported in both topaz-OH (Northrup et al., 1994) and in F and H bearing topaz (Gatta et al., 2006). Positions of the hydrogen atoms have also been reported using neutron diffraction study on fully deuterated topaz-OD ($Al_2SiO_4(OD)_2$) (Chen et al., 2005; Komatsu et al., 2008). We use the deuterated topaz-OD structure as our starting model (Komatsu et al., 2008). We however note that there are two distinct positions of protons with 0.5 occupancies i.e., the deuterium is disordered over D1 and D2 sites (Komatsu et al., 2008). Since our calculations are static, we consider five crystal structure models that are derived from the crystal structure refinement from neutron diffraction (Komatsu et al., 2008). In these crystal structure models, protons have full site occupancies, i.e., they are ordered. In our study, we use protons (H) instead of deuterium (D) atoms in all the crystal structure models. In the crystal structure model #1, all the protons occupy the H1 site. In the crystal structure model #2, all the protons occupy the H2 site. The resulting space group symmetry for both model #1 and #2 is *P*bmn (No. 62). Upon full geometry optimization we note that both crystal structure for model #1 and #2, both converge to an identical structure, where the proton occupies a position that is neither of the

Table 2
Equation of state parameters for topaz-OH and topaz-(F,OH).

V_0 (Å^3)	K_0 (GPa)	K'	Method
355.50 (n.r)	142.8 (n.r)	4*	SPXD[a]
343.32(±0.11)	154.0 (2.0)	4*	SCXD[b]
345.57 (±0.07)	158.0 (±4.0)	3.3 (±0.30)	SCXD[c]
345.57 (±0.07)	158.0 (±6.0)	3.3 (±0.40)	SCXD[d]
348.63 (±0.04)	164.7 (±0.04)	4.24 (±0.05)	GGA[e]
352.47 (±0.04)	166.4 (±0.6)	4.03 (±0.04)	GGA[f]

n.r.: not reported.
**fixed*.
[a] SPXD: Synchroton powder X-ray diffraction, $Al_2SiO_4(OH)_2$ (Grevel et al., 2000).
[b] SCXD: Single crystal X-ray diffraction, $Al_{2.01}Si_{1.0}O_{4.0}F_{1.57}(OH)_{0.43}$ (Komatsu et al., 2003).
[c] SCXD: Single crystal X-ray diffraction, $Al_{2.00}Si_{1.07}O_{4.00}F_{1.74}(OH)_{0.26}$ (Gatta et al., 2006).
[d] SCXD: Single crystal X-ray diffraction, $Al_{2.00}Si_{1.05}O_{4.00}F_{1.74}(OH)_{0.25}$ (Gatta et al., 2014).
[e] GGA: Monoclinic topaz-OH, GGA, $Al_2SiO_4(OH)_2$ (*this study*).
[f] GGA: Orthorhombic topaz-OH, GGA, $Al_2SiO_4(OH)_2$ (*this study*).

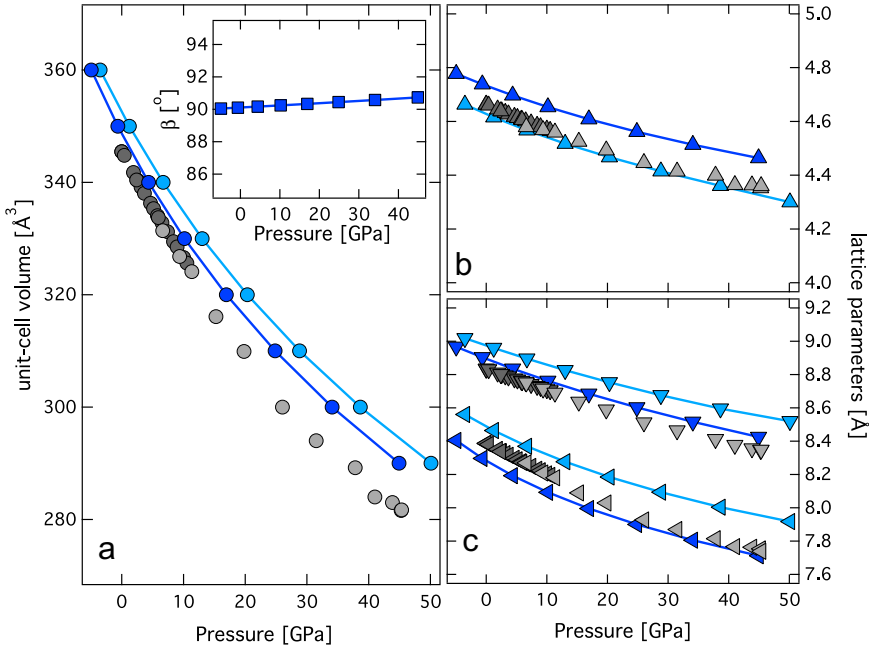

Fig. 2. (a) Pressure–volume results of topaz-OH, inset shows the variation of β as a function of pressure for the monoclinic topaz-OH, (b) Lattice parameters, *a*-, (c) *b*-, and *c*-axes as a function of pressures. Predictions from GGA (PAW)- monoclinic topaz-OH (dark blue filled symbols), orthorhombic topaz-OH (light blue filled symbols) are compared with experimental results- filled dark gray symbols (Gatta et al., 2006), filled light grey symbols (Gatta et al., 2014). (For interpretation of the references to colour in this figure legend, the reader is referred to the web version of this article.)

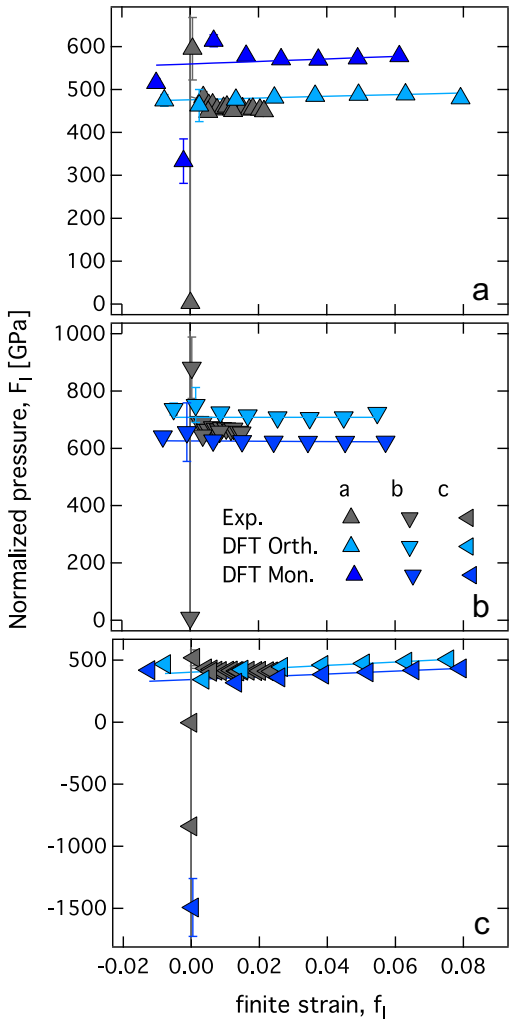

Fig. 3. Plot of linear normalized pressure (F_l) vs. Eulerian linear finite strain (f_l) from GGA (PAW) for (a) *a*-, (b) *b*- and (c) *c*-axis directions. Dark blue symbols – monoclinic topaz-OH, light blue symbols- orthorhombic topaz-OH, dark and light blue line- finite strain fits to GGA (PAW), gray symbols – single crystal X-ray diffraction results (Gatta et al., 2006), gray dashed line – finite strain fits using formulations as in (Chheda et al., 2014). (For interpretation of the references to colour in this figure legend, the reader is referred to the web version of this article.)

original H1 or H2 positions of the starting models (Table 1, Supplementary Figure 1). In the additional three crystal structure models, we have considered the protons fully occupied in a mix of H1 and H2 sites (Table 1). The resulting space group symmetry of the crystal structure model #3, #4, and #5 are $P2_1/c$ (No. 14), $P2_1/m$ (No. 11), and $P\bar{1}$ (No. 2) (Table 1, Supplementary Figure 1). Upon full geometry optimization, the crystal structure model #3 and model #5 converged to an identical crystal structure with a monoclinic space group symmetry $P2_1/c$ (No. 14). However, upon full geometry optimization, the crystal structure model #4 converged to a structure that has an orthorhombic symmetry *P*bnm (No. 62) and is identical with the geometrically optimized crystal structure from model #1 and model #2 (Table 1). So, although we began with five different model crystal structures, upon full relaxation and geometry optimization, we found two distinct crystal structures. The first one has an orthorhombic symmetry *P*bnm (No. 62) with a fully relaxed proton position H2′, which is distinct from H1 position but has slight similarity with the H2 proton position, except the y-fractional coordinate (Fig. 1, Table 1). The second crystal structure has a lower energy and has a monoclinic space group symmetry $P2_1/c$ with two distinct proton positions H1 and H2. However, these proton positions are fully occupied and have a Wyckoff symmetry of e and a site multiplicity of 4, i.e., (4e) (Figure 1, Supplementary Table 1a,b).

3. Results and discussion

3.1. Equation of state

The ground state energy of topaz-OH reveals that a crystal structure with an ordered hydrogen position i.e., monoclinic space group ($P2_1/c$) has lower energy than the topaz-OH with proton position in disordered position i.e., orthorhombic space group symmetry (*P*bmn) (Table 1). Our results confirms previous static calculations which also predicted lower energy for an ordered proton in a monoclinic symmetry topaz-OH(D) structure with $P2_1/b$ (i.e., $P2_1/c$ with *b* as the unique axis) over disordered protons in orthorhombic space group (*P*bmn) (Churakov and Wunder, 2004). Molecular dynamics studies and 3-D proton density distributions also showed that protons are likely to occupy H1 and H2 positions in an ordered configurations at lower temperatures (~55 K) and at higher temperatures (~270 K) protons are likely to exhibit significant disorder (Fig. 5b of Churakov and Wunder, 2004). Our results show that energy of the monoclinic topaz-OH remains lower than that of orthorhombic topaz-OH across all unit-cell volume explored in this study (Fig. 1). The volume dependence of total energy obtained using DFT simulations with GGA is adequately described by a third-order Birch–Murnaghan equation of state (Birch, 1978). The detailed expressions relating the total energy as a function of finite strain has been reported elsewhere (Chheda et al., 2014; Mookherjee and Tsuchiya, 2015a).

Table 3
Linear moduli, K_a, K_b, and K_c for topaz.

K_a [GPa]	(σK_a)	K_b	(σK_b)	K_c	(σK_c)	K_0'	($\sigma K_0'$)	K_0	(σK_0)	Stoichiometry	Method
495.0	(19.6)	704.2	(12.5)	444.4	(7.9)	175.7	(8.2)	154.0	(2.0)	$Al_{2.01}Si_{1.00}O_4F_{1.57}(OH)_{0.43}$	SCXD[a]
534.8	(2.9)	584.8	(2.1)	366.3	(1.3)	158.5	(1.2)	n.r.	n.r.	$Al_2SiO_4(OD)_{1.45}(OH)_{0.55}$	NPD[b]
152.0	(2.0)	224.0	(3.0)	137.0	(2.0)	54.5	(1.3)	164.0	(2.0)	$Al_{2.00}Si_{1.05}O_{4.00}F_{1.75}(OH)_{0.26}$	SCXD[c]
483.4	(0.1)	696.3	(0.03)	434.6	(0.1)	172.2	(0.0)	164.0	(2.0)	$Al_{2.00}Si_{1.05}O_{4.00}F_{1.75}(OH)_{0.26}$	SCXD[d]
559.6	(3.4)	625.7	(3.7)	342.6	(2.6)	158.6	(1.8)	164.7	(0.7)	$Al_2SiO_4(OH)_2$	GGA[e]
477.9	(3.6)	695.5	(9.7)	411.0	(6.8)	167.7	(3.8)	166.4	(0.6)	$Al_2SiO_4(OH)_2$	GGA[f]

n. r. – not reported.
[a] SCXD: single crystal X-ray Diffraction (Komatsu et al., 2003).
[b] NPD: Neutron powder diffraction (Komatsu et al., 2008).
[c] SCXD: single crystral X-ray diffraction (Gatta et al., 2006).
[d] Re-analysis of single crystal X-ray data from Gatta et al. (2006) using linear finite strain equations as described in Mookherjee and Bezacier (2012).
[e] GGA: Monoclinic topaz-OH, Generalized gradient approximation (*this study*) note K_c refers to compressibility along the $c' = c \sin\beta$ component.
[f] GGA: Orthorhombic topaz-OH, Generalized gradient approximation (*this study*).

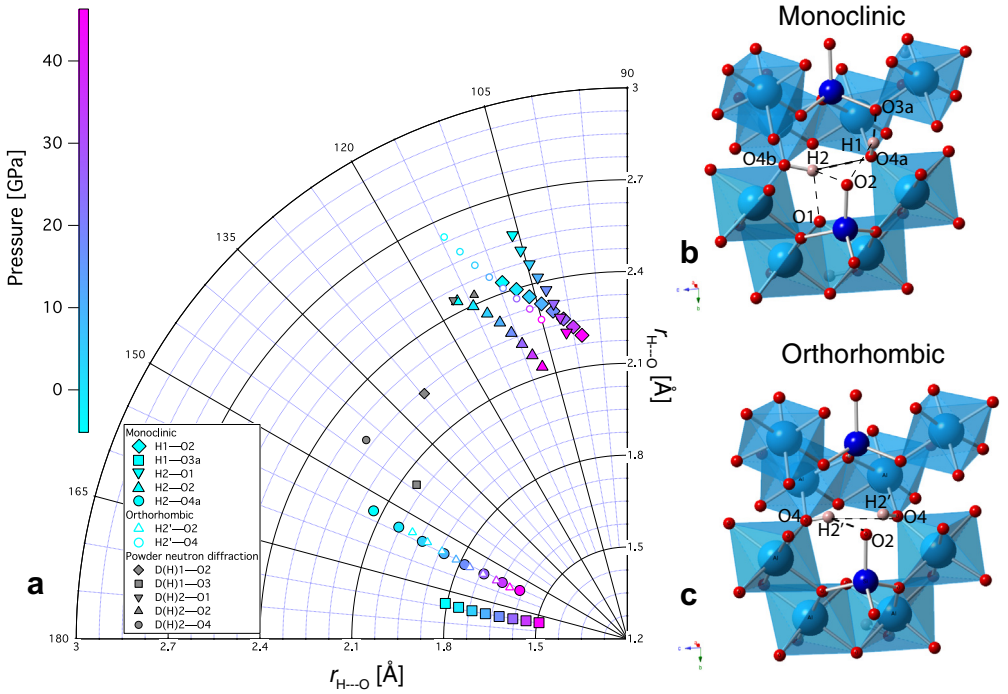

Fig. 4. (a) Hydrogen bond configurations plotted in a polar plot of d(H···O) vs O–H···O angles. The filled colored symbols are from monoclinic topaz-OH, the open colored symbols are from orthorhombic topaz-OH. The symbols are color contoured with the pressure. The pressure scale is shown in the left-hand side of the polar graph. The gray symbols are from neutron powder diffraction study (Komatsu et al., 2008), (b) the local structure of monoclinic topaz-OH highlighting the local O4a–H1 and O4b–H2 geometry, (c) the local structure of orthorhombic topaz-OH highlighting the O4–H2′ geometry. For the atom labels of the orthorhombic and monoclinic topaz-OH, please refer to the supplementary Table ST1. (For interpretation of the references to colour in this figure legend, the reader is referred to the web version of this article.)

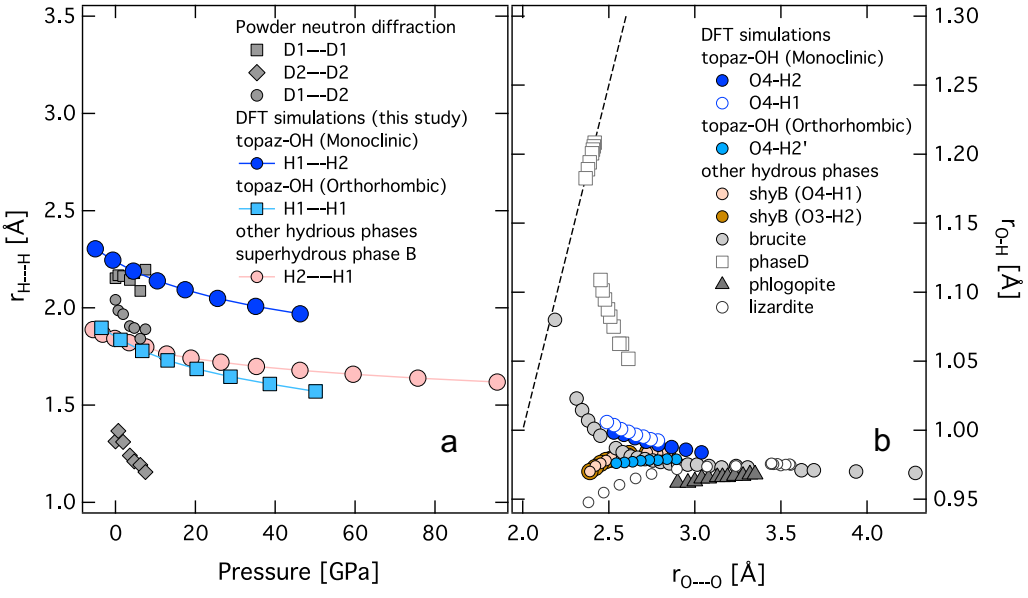

Fig. 5. (a) Plot of H···H non bonded interactions in topaz-OH and other hydrous phases. (b) Plot of r_{O-H} as a function of $r_{O\cdots O}$ for topaz-OH and other hydrous phases. The dashed line represents the condition for symmetric hydrogen bond where r_{O-H} is equal to half of $r_{O\cdots O}$. Only phase-D (Tsuchiya and Tsuchiya, 2009) exhibits symmetric hydrogen bonding. Symmetric hydrogen bonding in brucite could be achieved at pressures beyond its thermodynamic stability (Mookherjee and Stixrude, 2006). Phases such as lizardite (Mookherjee and Stixrude, 2009), superhydrous phase B (Mookherjee and Tsuchiya, 2015a), chlorite (Mookherjee and Mainprice, 2014), phlogopite (Chheda et al., 2014) do not show hydrogen bonding since r_{O-H} do not show any evidence of stretching upon compression. Monoclinic topaz-OH however shows stretching of O4a–H1 and O4b–H2 upon compression.

The zero-pressure unit-cell volume for the monoclinic topaz-OH based on the GGA, V_0^{mon} is 348.63 (±0.04) Å^3, i.e., ~0.9% larger than the zero-pressure volume based on single crystal X-ray diffraction study, V_0^{exp} (Gatta et al., 2006). The zero-pressure bulk-modulus based for the monoclinic topaz-OH based on the GGA, K_0^{mon}, is 164.7 (±0.04) GPa, i.e., 4% larger than the zero-pressure bulk-modulus based on single crystal X-ray diffraction study, V_0^{exp} (Gatta et al., 2006). In comparison, the zero-pressure unit-cell volume (V_0^{orth}) and zero pressure bulk modulus (V_0^{orth}) for the orthorhombic topaz-OH based on the GGA, are 352.47

(±0.04) Å^3 and 166.4 (±0.6) GPa respectively, i.e., V_0^{orth} is 2% larger and K_0^{orth} is 5% larger than those determined by single crystal X-ray diffraction study (Gatta et al., 2006) (Fig. 2, Table 2). This discrepancy between the zero-pressure volume and bulk-modulus is related to a combination of factors including (a) comparison of 0 K DFT results with 300 K experimental results and (b) the GGA tends to under-bind the condensed matter phases and hence predicts larger zero-pressure volumes and smaller bulk modulus. One of the plausible reasons that first principles simulation based on DFT and GGA predicts a stiffer zero pressure bulk modulus is likely to be related to the difference in chemistry of the topaz-OH examined in this study ($Al_2SiO_4(OH)_2$) versus the experimental sample. The single-crystal examined in the experimental studies have significant fluorine substitution in the hydroxyl site with a resulting stoichiometry of $Al_2SiO_4(F_{1.75}(OH)_{0.26})$ (Gatta et al., 2006, 2014). The pressure dependence of the unit-cell volume for monoclinic topaz-OH agrees nicely with the experimental results up to pressures of 15 GPa (Fig. 2).

The lattice parameters obtained for the monoclinic topaz-OH i.e., a^{mon}, b^{mon}, and c^{mon}, shortens upon compression. The β^{mon} angle remains close to ~90° and differs from 90° by less than 1° at compressions up to 40 GPa indicating that the monoclinic distortion is rather insignificant (Fig. 2). The orthorhombic topaz-OH a^{orth} lattice parameter agrees better with the experimental results, whereas the monoclinic topaz-OH b^{mon}, and c^{mon} agrees better with the experimental results (Fig. 2). The linear bulk moduli for both monoclinic and orthorhombic topaz-OH were determined using linear finite strain expression (Chheda et al., 2014; Davies, 1974; Mookherjee and Tsuchiya, 2015a; Weaver, 1976; Wentzcovitch and Stixrude, 1997) and linear Eulerian finite strain and linear normalized pressures (Fig. 3, Table 3). For the orthorhombic topaz-OH, the linear moduli along a^{orth}-, b^{orth}-, and c^{orth}-axis directions follow the relation $K_b^{orth} > K_a^{orth} > K_c^{orth}$. For the monoclinic topaz-OH, the linear moduli along a^{mon} -, b^{mon}-, and a'^{mon}-axis directions follow the relation $K_b^{mon} > K_a^{mon} > K_c'^{mon}$, where c'^{mon} refers to $c'^{mon} \times sin\beta^{mon}$, however, it is to be noted that $\beta^{mon} \sim 90°$ at most of the pressures (Fig. 2), i.e., $sin\beta^{mon} \sim 1$ at most of the pressures. Our calculated results for both orthorhombic and monoclinic topaz-OH are in agreement with the trends observed in compression studies of single crystal topaz with $K_b^e xp > K_a^e xp > K_c^e xp$ (Komatsu et al., 2003; Gatta et al., 2006) (Table 3). Although, the trends in the linear moduli are similar between the simulations and experiments, the magnitude of the linear compressibility ($\beta_l = \frac{1}{K_l}$) along *a*-, *b*-, and *c*-axis directions, reported in previous experimental studies and the simulations differ significantly (Table 3). Based on our DFT simulations, the linear moduli for the orthorhombic topaz-OH, i.e., K_a^{orth}, K_b^{orth}, and K_c^{orth} are 478, 696, and 411 GPa whereas the linear moduli for the monolionic topaz-OH, i.e., K_a^{mon}, K_b^{mon}, and K_c^{mon} are 560, 626, and 343 GPa. This is in contrast with the experimentally determined linear moduli K_a^{exp}, K_b^{exp}, and K_c^{exp} of 152, 224, and 137 GPa (Gatta et al., 2006). However, our results on monoclinic and orthorhombic topaz-OH are in better agreement with an earlier single crystal X-ray diffraction study with linear moduli K_a^{exp}, K_b^{exp}, and K_c^{exp} of 495, 704, and 444 GPa (Komatsu et al., 2003). Based on the present DFT study,

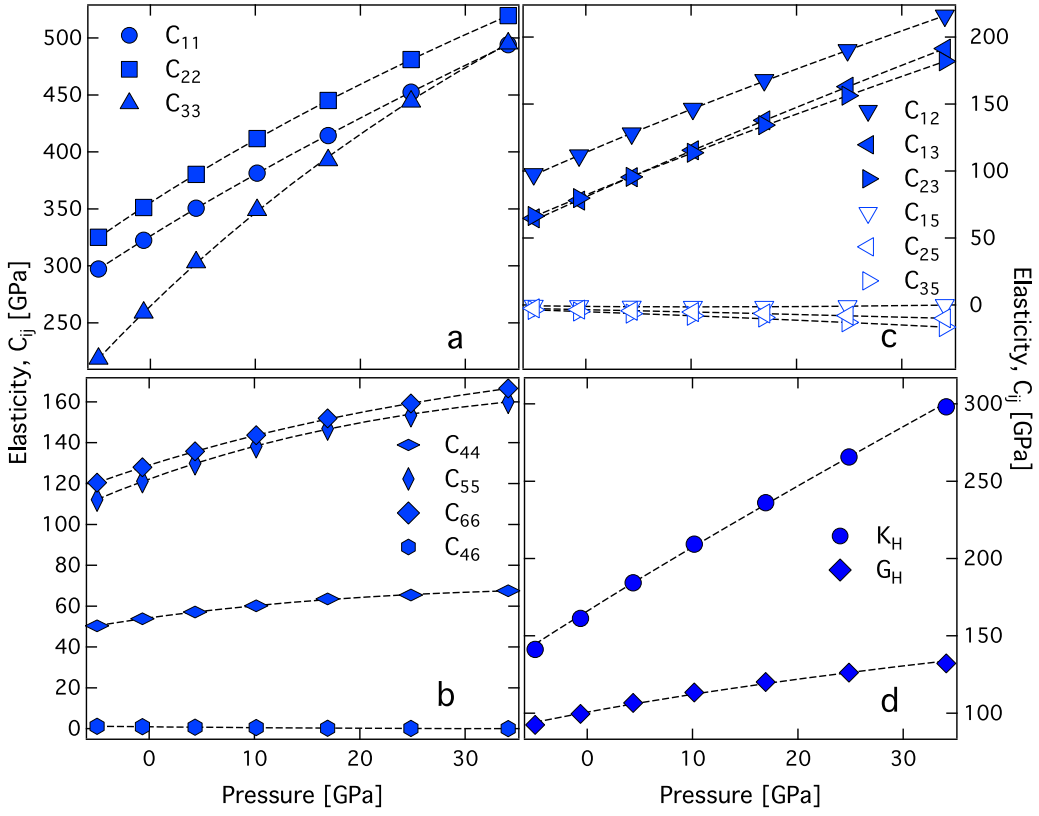

Fig. 6. Elastic constants, c_{ij} for the monoclinic topaz-OH as a function of pressure- (a) compressional elastic constants-c_{11}^{mon}, c_{22}^{mon}, c_{33}^{mon}, (b) off-diagonal elastic constants-c_{12}^{mon}, c_{13}^{mon}, c_{23}^{mon}, c_{15}^{mon}, c_{25}^{mon}, c_{35}^{mon}, (c) shear elastic constants-c_{44}^{mon}, c_{46}^{mon}, c_{55}^{mon}, c_{66}^{mon} and (d) Voigt-Reuss-Hill averaged bulk, K_H^{mon} and shear, G_H^{mon}, moduli. All the data are reported in (Table 4). Dark blue symbols – GGA (PAW) predictions, black dashed line represents finite strain fit as described in Chheda et al. (2014), Karki et al. (2001), Mookherjee and Tsuchiya (2015a). (For interpretation of the references to colour in this figure legend, the reader is referred to the web version of this article.)

the bulk modulus ($K_0 = \frac{1}{\beta_0}$) estimated from the linear moduli, i.e., using the relation, $\beta_0 = [\beta_a + \beta_b + \beta_c]$ yields 168 and 159 GPa for the orthorhombic and monoclinic topaz-OH respectively. This is consistent with the zero-pressure bulk modulus derived using the formulation of finite strain dependence of energy (Tables 2 and 3). However, the bulk modulus ($K + 0^{exp}$) estimated from the linear moduli is 54.5 GPa as opposed to the reported zero-pressure bulk modulus of 164 GPa using the Birch–Murnaghan finite strain formulation on the pressure–volume data (Gatta et al., 2006) (Table 3). The discrepancy is likely related to the erroneous linearization of the volume finite strain formulation and defining the linear compressibility as $\beta_l = \frac{1}{3K_o(l)}$, where $K_o(l)$ is the zero-pressure bulk modulus obtained by using the Birch–Murnaghan finite strain formulation on the lattice parameter-pressure data, cubing the lattice parameter as a isotropic volume (Gatta et al., 2006). Instead, by using the linear finite strain formulation (Chheda et al., 2014; Davies, 1974; Mookherjee and Tsuchiya, 2015a; Weaver, 1976; Wentzcovitch and Stixrude, 1997) we find agreeable results that are both consistent with the bulk modulus and are also consistent with DFT results and the previous experiments (Komatsu et al., 2003) (Table 3).

3.2. Behavior of hydrogen atoms in topaz-OH

DFT studies based on GGA indicate that the monoclinic topaz-OH exhibits bent and tri- or bi-furcated hydrogen bond configurations (Fig. 4). The monoclinic topaz-OH has two distinct hydrogen positions H1 and H2. The O4a–H1 forms hydrogen bonds with O2 and O3a atoms. The O2 atom is located at the apex of the silicon tetrahedral, whereas the O3a atom is located at the base of the silicon tetrahedral unit. The O4b–H2 forms tri-furcated hydrogen bond with O1, O2, and O4a atoms. Based on the O–H···O angles the O4a–H1···O2, O4b–H2···O1, and O4b–H2···O2 bonds have significantly bent configurations ranging from 105° to 115°. In contrast, the O4a–H1···O3a and O4b–H2···O4a have bond angles ranging between 155° and 170° making them likely candidates for stronger hydrogen bonds. The H1···O3a distance is one of the shortest distance making it the strongest hydrogen bond candidate among the rest of the H···O units (Fig. 4). The trends observed in our study are in good agreement with previous neutron diffraction study (Komatsu et al., 2008). However, the details differ since the monoclinic symmetry allows greater flexibility for the full relaxation of the hydrogen position resulting in greater O–H···O angles for the O4a–H1···O3a and O4b–H2···O4a pairs. DFT studies based on GGA for the orthorhombic topaz-OH has a single hydrogen environment with O4–H2′ forming a bifurcated hydrogen bond with the O2 and the O4 atoms (Fig. 4). Based on the O–H···O geometry, the O4–H2′···O2 seems to be a better candidate for stronger hydrogen bonding. The non-bonded hydrogen–hydrogen repulsive interaction for the orthorhombic topaz-OH, i.e., d(H2′···H2′) is lower than the repulsive interactions in the monoclinic topaz-OH, i.e., d(H1···H2) (Fig. 5). The greater H1···H2 distance ensures minimal repulsive strain in the monoclinic topaz-OH. The lower H1···H2 distance is likely to be achieved by tilting of the O–H dipole and formation of stronger hydrogen bonds. Formation of hydrogen bonds upon compression could also be examined by following the relationship between the r_{O-H} and $r_{O\cdots O}$. Upon compression, in a O–H···O unit, the $r_{O\cdots O}$ distance is likely to reduce, whereas if the acceptor oxygen atom draws the hydrogen atom towards itself by forming hydrogen bond, the r_{O-H} bond distance is likely to increase. This has been observed in hydrous minerals exhibiting strong hydrogen bonds, for instance, phase-D and brucite (Fig. 5). In the monoclinic topaz-OH, the r_{O4a-H1} and r_{O4b-H2} bonds in tend to increase upon compression as the $r_{O4a\cdots O3a}$ $r_{O4b\cdots O4a}$ bond length reduces indicating that these two O–H···O units form hydrogen

Table 4
Unit-cell volume, density (ρ), full elastic constant tensor (C_{ij}), Hill averages of bulk (K_H) and shear (G_H) modulus, compressional wave (AV_P) and shear wave (AV_S) anisotropy and velocities (V_P, V_S) of monoclinic topaz-OH as a function of pressure.

V [Å^3]	ρ [g/cm^3]	P [GPa]	C_{11}	C_{22}	C_{33}	C_{12}	C_{13}	C_{23}	C_{15}	C_{25}	C_{35}	C_{44}	C_{55}	C_{66}	C_{46}	K_H	G_H	AV_P [%]	AV_S	V_P [km/s]	V_S
360.0	3.32	−4.9	297.2	325.1	218.7	97.6	64.6	66.4	−0.6	−2.4	−3.6	50.3	112.1	120.4	1.2	141.2	92.4	23.2	43.0	8.92	5.27
350.0	3.42	−0.6	322.4	351.3	258.9	111.6	77.9	79.8	−0.9	−3.4	−4.9	53.8	121.1	128.0	1.0	161.2	99.5	20.1	42.7	9.28	5.40
340.0	3.52	4.4	350.6	380.3	303.2	128.1	95.4	95.6	−1.2	−4.3	−6.4	57.1	129.9	135.8	0.7	184.3	106.6	17.8	42.7	9.63	5.50
330.0	3.62	10.2	381.3	411.7	349.1	146.4	115.4	113.6	−1.3	−5.3	−8.0	60.1	138.2	143.6	0.5	209.3	113.4	15.9	42.9	9.97	5.59
320.0	3.74	16.9	414.3	445.2	392.7	167.8	137.8	134.2	−1.3	−6.3	−9.3	63.5	146.9	151.9	0.2	236.1	120.1	14.7	42.9	10.30	5.67
310.0	3.86	24.8	452.4	481.0	444.1	190.1	162.9	156.2	−0.9	−7.9	−12.9	65.4	153.4	159.2	0.2	265.6	126.3	13.7	43.8	10.61	5.72
300.0	3.99	34.1	494.1	519.6	495.2	215.9	191.4	181.8	0.0	−9.9	−16.4	67.5	160.0	166.6	0.0	298.1	132.2	12.7	44.4	10.91	5.76
Finite strain fit																					
348.6	3.43	0	326.2 (5.7)	355.5 (5.9)	264.7 (8.9)	113.8 (3.3)	80.7 (3.5)	82.0 (3.2)	−1.0 (−0.1)	−3.5 (−0.2)	−5.0 (−0.3)	54.2 (0.7)	122.2 (1.9)	129.0 (1.6)	0.9 (0.001)	166.0 (4.2)	100.8 (1.2)	19.7	42.7	9.51	5.51

bonds upon compression. However, in the orthorhombic topaz-OH, the $r_{O4-H2'}$ bond length reduces upon compression indicating that hydrogen bonding is likely to be weak in this configuration. Based on the H2′···H2′ non-bonded interaction and the reduction of the O4–H2′ distance, it is likely that fluorine substitution would reduce the repulsive strain in a topaz with H2' hydrogen position.

3.3. Elasticity

The monoclinic topaz-OH has 13 independent elastic constants, with three compressional elastic constants-c_{11}^{mon}, c_{22}^{mon}, c_{33}^{mon}, six off-diagonal elastic constants-c_{12}^{mon}, c_{13}^{mon}, c_{23}^{mon}, c_{15}^{mon}, c_{25}^{mon}, c_{35}^{mon} and four shear elastic constants-c_{44}^{mon}, c_{46}^{mon}, c_{56}^{mon}, c_{66}^{mon} (Nye, 1985). Upon compression, most of the principal, off-diagonal, and shear elastic constants stiffen (Fig. 6, Table 4). Only c_{15}^{mon}, c_{25}^{mon}, c_{35}^{mon} have slight negative pressure dependence (Table 4). At low pressures, $c_{22}^{mon} > c_{11}^{mon} > c_{33}^{mon}$, this is consistent with the relationship between linear bulk moduli $K_b^{mon} > K_a^{mon} > K_c^{mon}$ (Fig. 3). However, upon compression the relationship among the principal elastic constants evolves to $c_{22}^{mon} > c_{11}^{mon} \sim c_{33}^{mon}$ (Fig. 6, Table 4). Across the entire pressure range explored in this study, $c_{44}^{mon} < c_{55}^{mon} \sim c_{66}^{mon}$ (Fig. 6, Table 4). At low pressures, $c_{12}^{mon} > c_{23}^{mon-GGA} \geq c_{13}^{mon}$, however, upon compression, the relationship changes to $c_{12}^{mon} > c_{13}^{mon} > c_{23}^{mon}$ (Fig. 6, Table 4).The orthorhombic topaz-OH has 9 independent elastic constants, three compressional elastic constants-c_{11}^{orth}, c_{22}^{orth}, c_{33}^{orth}, three off diagonal elastic constants-c_{12}^{orth}, c_{13}^{orth}, c_{23}^{orth} and three

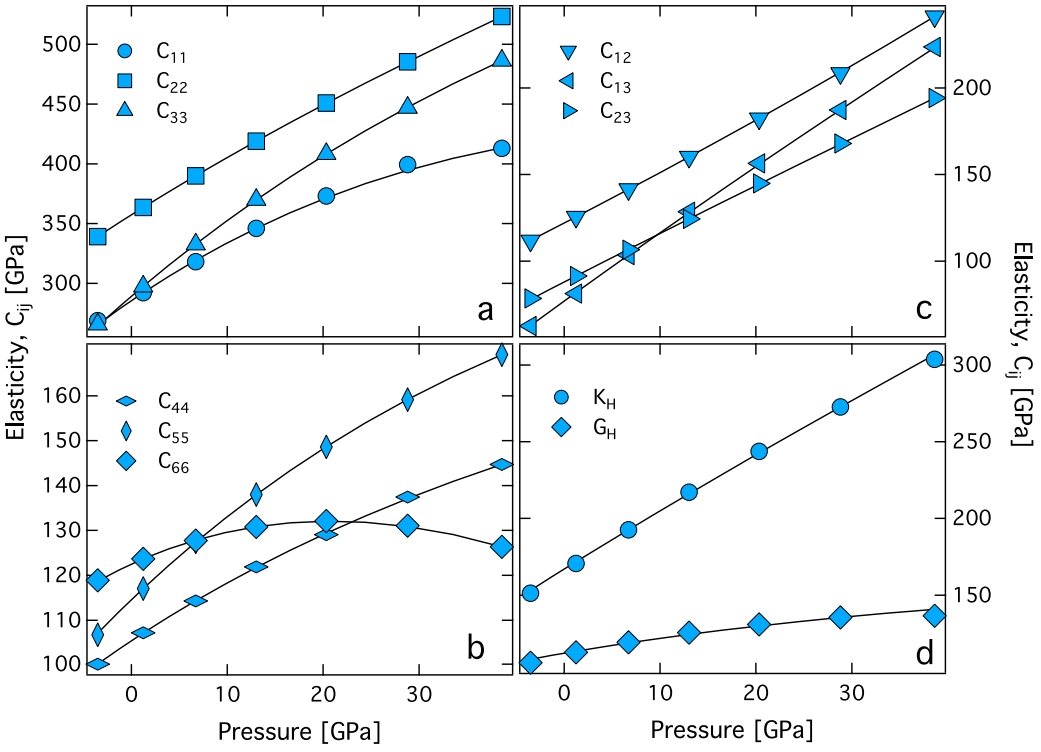

Fig. 7. Elastic constants, c_{ij} for the orthorhombic topaz-OH as a function of pressure- (a) compressional elastic constants-c_{11}^{orth}, c_{22}^{orth}, c_{33}^{orth}, (b) off-diagonal elastic constants-c_{12}^{orth}, c_{13}^{orth}, c_{23}^{orth} (c) shear elastic constants-c_{44}^{orth}, c_{55}^{orth}, c_{66}^{orth}, and (d) Voigt-Reuss-Hill averaged bulk, K_H^{orth} and shear, K_G^{orth}, moduli. All the data are reported in (Table 5). Light blue symbols – GGA (PAW) predictions, black line represents finite strain fit as described in Chheda et al. (2014), Karki et al. (2001), Mookherjee and Tsuchiya (2015a). (For interpretation of the references to colour in this figure legend, the reader is referred to the web version of this article.)

Table 5
Unit-cell volume, density (ρ), full elastic constant tensor (C_{ij}), Hill averages of bulk (K_H) and shear (G_H) modulus, compressional wave (AV_P) and shear wave (AV_S) anisotropy and velocities (V_P, V_S) of orthorhombic topaz-OH as a function of pressure.

V	ρ	P	C_{11}	C_{22}	C_{33}	C_{12}	C_{13}	C_{23}	C_{44}	C_{55}	C_{66}	K_H	G_H	AV_P	AV_S	V_P	V_S
[Å^3]	[g/cm^3]	[GPa]												[%]		[km/s]	
360	3.32	−3.5	268.9	339.2	265.7	111.8	62.5	78.5	100.2	106.8	118.9	151.2	105.9	12.3	8.5	9.38	5.65
350	3.42	1.2	292.2	363.5	297.4	125.5	81.2	91.4	107.2	117.0	123.7	170.6	112.7	11.0	8.5	9.69	5.74
340	3.52	6.7	318.2	389.9	332.7	141.4	103.5	106.6	114.3	127.5	127.8	192.6	119.2	10.2	9.5	10.00	5.82
330	3.62	13.0	346.0	418.9	370.0	160.2	128.5	124.4	121.9	138.0	130.8	217.1	125.6	10.8	10.5	10.30	5.89
320	3.74	20.3	373.1	450.8	408.3	182.3	156.5	144.8	129.1	148.6	132.1	243.7	131.0	11.0	11.8	10.58	5.92
310	3.86	28.8	399.3	485.4	447.0	208.4	187.3	167.9	137.5	159.1	131.1	272.6	135.4	9.7	13.4	10.84	5.93
300	3.99	38.6	413.0	523.2	486.4	241.2	223.7	194.2	144.7	169.2	126.3	303.7	136.5	11.8	18.0	11.04	5.85
Finite strain fit																	
352	3.39	0	285.6 (5.5)	357.3 (5.1)	289.2 (6.9)	122.0 (2.9)	76.9 (4.0)	87.9 (2.9)	105.4 (1.4)	114.6 (2.1)	122.5 (1.0)	166.9 (4.0)	112.1 (1.1)	11.3	8.4	9.66	5.75
$Al_2SiO_4F_2$[a]																	
	3.56	0	278.8	344.8	292.3	120.4	80.6	80.3	108.6	132.9	130.3	163.2	111.1	12.0	13.7	9.35	5.59

[a] Ultrasonic resonance along different orientations (Haussühl, 1993).

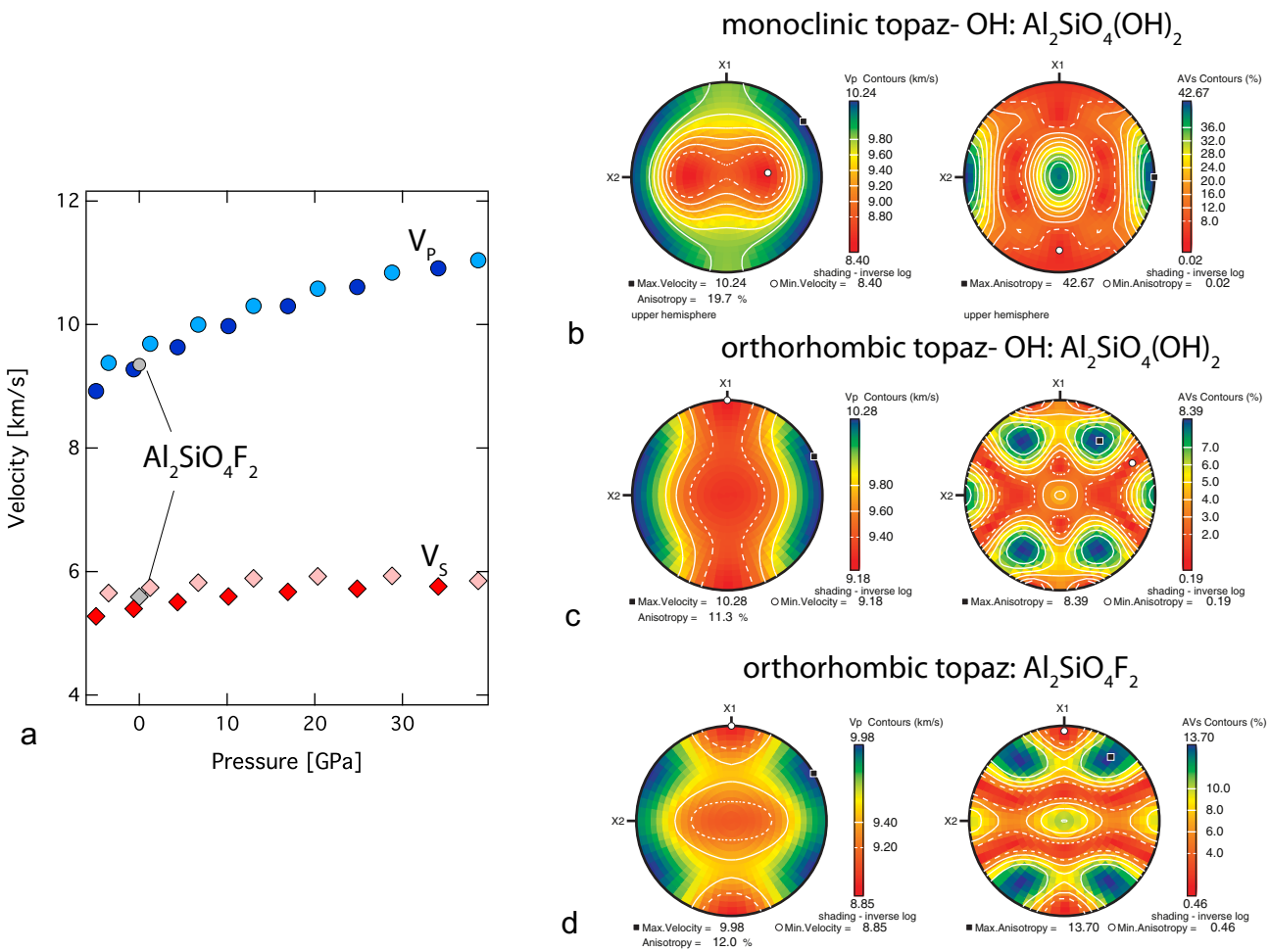

Fig. 8. (a) Plot of compressional wave V_P and shear wave velocity, V_S for topaz-OH, as a function of pressure. The dark blue and dark red filled symbols are for the compressional (V_P^{mon}) and shear wave (V_S^{mon}) velocity for the monoclinic topaz-OH. The light blue and light red filled symbols are for the compressional (V_P^{orth}) and shear wave (V_S^{orth}) velocity for the monoclinic topaz-OH. Also shown are the V_P^{exp} and V_S^{exp} for the fluorine end member topaz at 1 bar. (b) The azimuthal compressional wave anisotropy (AV_P^{mon}) and shear wave anisotropy (AV_S^{mon}) for the monoclinic topaz-OH, (c) the azimuthal compressional wave anisotropy (AV_P^{mon}) and shear wave anisotropy (AV_S^{mon}) for the orthorhombic topaz-OH from this study, and (d) the azimuthal compressional wave anisotropy (AV_P^{exp}) and shear wave anisotropy (AV_S^{exp}) for the fluorine end member $Al_2SiO_4F_2$ at 1 bar (Haussühl, 1993). (For interpretation of the references to colour in this figure legend, the reader is referred to the web version of this article.)

shear elastic constants c_{44}^{orth}, c_{55}^{orth}, c_{66}^{orth} (Fig. 7, Table 5). We note that the hill averaged bulk moduli of monoclinic (K_H^{mon}) and orthorhombic (K_H^{mon}) topaz-OH differ by less than 1 GPa i.e., 0.5%, whereas the hill averaged shear modulus of monoclinic (G_H^{mon}) and orthorhombic (G_H^{orth}) topaz-OH differ by more than 11 GPa i.e., 10% indicating that the shear modulus is more sensitive to the proton configurations and symmetry of the topaz-OH crystal structure (Tables 4 and 5). So far, we are not aware of any full elastic constant tensor results on hydrogen bearing end-member topaz-OH. The calculated elastic constants for orthorhombic topaz-OH at room pressure (0 GPa) are in good agreement with the experimental results of full elastic constant tensor on fluorine end-member of topaz (Haussühl, 1993) (Table 5).

4. Conclusion

The elasticity and compressibility of topaz can be rationalized in terms of the crystal structure and the response of the individual polyhedral units upon compression. The topaz-OH crystal structure consists of edge sharing AlO_6 octahedral units and corner sharing SiO_4 tetrahedral units. In monoclinic topaz-OH, the SiO_4 tetrahedral units remains rigid and the polyhedral volume could be well described by a finite strain formulations with zero-pressure bulk modulus, $K_0^{mon-SiO_4}$ of 314.7 (±3.9) GPa, a zero-pressure polyhedral volume, $V_0^{mon-SiO_4}$ of 2.3229 (±0.0006) Å^3, and a pressure derivative of bulk modulus, $K_0'^{mon-SiO_4}$ of 6.9 (±0.3). Similar to the monoclinic topaz-OH, the SiO_4 units in orthorhombic topaz-OH remain rigid. The compressibility parameters for the tetrahedral units in orthorhombic topaz-OH could be described with a zero-pressure bulk modulus, $K_0^{orth-SiO_4}$ of 329.8 (±5.7) GPa, zero-pressure polyhedral volume, $V_0^{orth-SiO_4}$ of 2.3249 (±0.0009) Å^3, and the pressure derivative of bulk modulus, $K_0'^{orth-SiO_4}$ of 5.6 (±0.3). The AlO_6 octahedral units are relatively softer. In the monoclinic topaz-OH, the AlO_6 units could be described with a finite strain formulation with zero-pressure bulk modulus, $K_0^{mon-AlO_6}$ of 215.2 (±1.7) GPa, a zero-pressure polyhedral volume, $V_0^{mon-AlO_6}$ of 9.0991 (±0.0023) Å^3, and a pressure derivative of bulk modulus, $K_0'^{mon-AlO_6}$ of 4.9 (±0.1). In the orthorhombic topaz-OH, the AlO_6 polyhedral units could be described with a finite strain formulation with zero-pressure bulk modulus, $K_0^{orth-AlO_6}$ of 219.3 (±0.7) GPa, zero-pressure polyhedral volume, $V_0^{orth-AlO_6}$ of 9.0749 (±0.0009) Å^3, and a pressure derivative of bulk modulus, $K_0'^{orth-AlO_6}$ 4.7 (±0.04). Since the tetrahedral units are considerably rigid compared to the octahedral units, there are weaker zones in-between

the tetrahedral units, and are parallel to the *a*–*b* plane, i.e., (001) planes and perpendicular to the *c*-axis, i.e., [001] direction. These weaker zones or cleavages have been recognized in earlier studies of topaz (Ribbe and Gibbs, 1971; Gatta et al., 2014). Owing to these weaker zones, compressibility along the [001] direction is softer compared to the compressibility along [010] direction (Table 3). This is also consistent with the predictions for the principal components of the full elastic constant tensors (Tables 4 and 5).

The predicted sound wave velocity and the full elastic constant tensor for topaz-OH with $Al_2SiO_4(OH)_2$ stoichiometry show considerable anisotropy. For the monoclinic topaz-OH, the predicted P-wave azimuthal anisotropy, $AV_P^{mon} \sim 19.7\%$ and S-wave anisotropy, $AV_S^{mon} \sim 42.7\%$ at 1 bar (Fig. 8). In contrast, for the orthorhombic topaz-OH the predicted P-wave azimuthal anisotropy, $AV_P^{orth} \sim 11.3\%$ and S-wave anisotropy, $AV_P^{orth} \sim 8.4\%$ at 1 bar (Fig. 8). The predicted P- and S-wave anisotropy for the orthorhombic topaz-OH at 1 bar is in good agreement with the experimental study on fluorine end member with $Al_2SiO_4F_2$ stoichiometry (Haussühl, 1993) (Fig. 8). The P-wave azimuthal and S-wave anisotropy anisotropy with the fluorine end member topaz is slightly greater with AV_P^{exp} is ~12.0% and $AV_S^{exp} \sim 13.7\%$ at 1 bar. Based on the similarity of P- and S-wave anisotropy, it is likely that the hydrogen atom position and the OH dipole orientation in a F, OH bearing topaz is similar to the orthorhombic topaz-OH hydrogen positions. Both the anisotropy and the shear elastic constants are sensitive to the hydrogen position and OH dipole orientation.

A simplified ASH ternary representative of the alumina and silica rich subducting sediment layer along a cold geothermal gradient (<4 °C/km), is likely to stabilize layered hydrous aluminosilicates such as kaolinite, which has low density, compressional (V_P) and shear (V_S) velocity. As these hydrous phases are dragged to greater depths, they dehydrate and stabilizes a mixture of disapore and oesite. Diaspore is denser and has greater compressional (V_P) and shear (V_S) velocity. As diaspore decomposes, it is likely to stabilize mineral phases such as phase-pi and topaz-OH (Wunder et al., 1993a,b; Schreyer, 1995). We note that both monoclinic and orthorhombic topaz-OH have greater zero pressure density compared to diaspore, i.e., $\rho_0^{dia} < \rho_0^{orth-topOH} < \rho_0^{mon-topOH}$ (Table 6, Fig. 9). Our DFT results reveal that the compressional and shear wave velocity of topaz-OH varies

Table 6
Density, compressional (V_P), and shear (V_S) wave velocity of mineral phases in Al_2O_3–SiO_2–H_2O ternary.

Mineral	Abbreviation	Formula	ρ [g/cm^3]	V_P [km/s]	V_S [km/s]	References
Corundum	cor	Al_2O_3	3.98	10.88	6.40	Ohno et al. (1986)
Quartz	qz	SiO_2	2.64	6.09	4.12	Ohno et al. (2006)
Coesite	cs	SiO_2	2.93	8.17	4.58	Weidner and Carleton (1977)
Ice	ice-iii	H_2O	1.16	3.66	2.01	Tulk et al. (1994)
Andalusite	and	Al_2SiO_5	3.15	9.76	5.65	Vaughan and Weidner (1978)
Sillimanite	sil	Al_2SiO_5	3.24	9.65	5.42	Vaughan and Weidner (1978)
Kyanite	ky	Al_2SiO_5	3.76	9.68	5.87	Winkler et al. (2001)
Diaspore	dia	AlOOH	3.38	9.42	5.83	Jiang et al. (2008)
Kaolinite	kl	$Al_2Si_2O_5(OH)_4$	2.52	6.23	3.55	Katahara (1996)
Topaz	*mon*-top-OH	$Al_2SiO_4(OH)_2$	3.43	9.75	5.81	this study
Topaz	*orth*-top-OH	$Al_2SiO_4(OH)_2$	3.39	9.51	5.51	this study

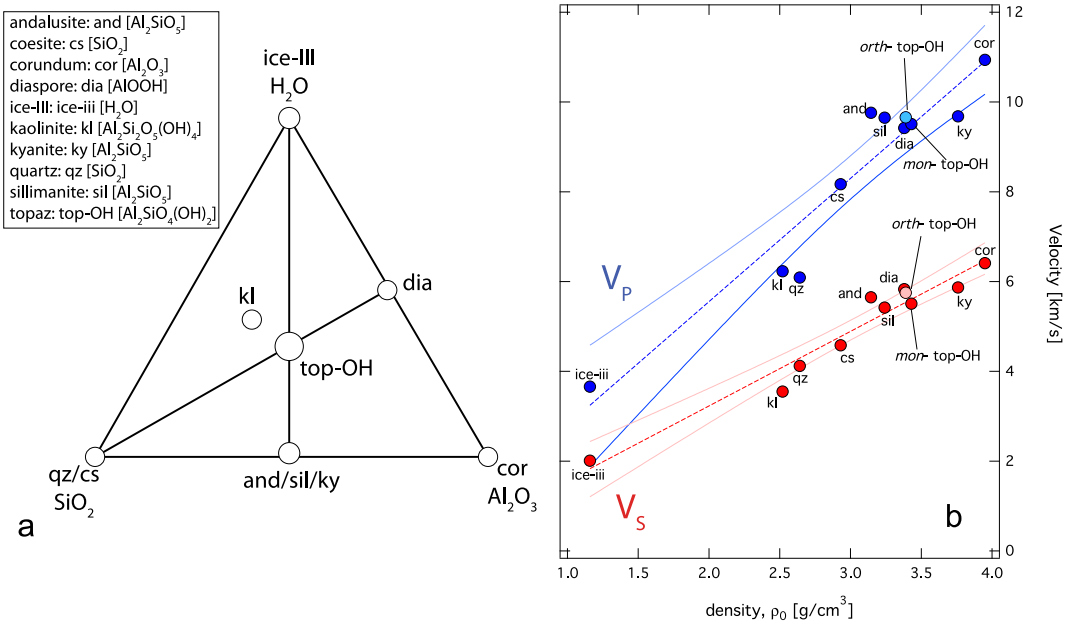

Fig. 9. (a) A ternary plot showing the Al_2O_3–SiO_2–H_2O components that are relevant for the mineral phases that are stable in subducted sediments. The end member components considered in this study are SiO_2 component with quartz (qz) and coesite (cs) polymorphs; Al_2O_3 component with corundum (cor), H_2O component with ice-III. Intermediate phases andalusite (and), silimanite (sil), and kyanite (ky) are polymorphs with Al_2SiO_5 stoichiometry, diaspore (dia) has AlOOH stoichiometry, kaolinite (kl) with $Al_2Si_2O_5(OH)_4$ stoichiometry, and $Al_2SiO_4(OH)_2$ stoichiometry refers to topaz-OH. (b) plot of V_P and V_S as a function of density. The blue and red dashed line represents linear regression fits for compressional wave [$V_P = 2.75(\pm0.66)\ \rho + 0.06(\pm2.07)$] and shear wave [$V_S = 1.66(\pm0.30)\ \rho + 0.09(\pm0.94)$] respectively. The light blue and red lines represents 95% confidence level for the primary and shear velocity- density regressions. (For interpretation of the references to colour in this figure legend, the reader is referred to the web version of this article.)

as a function of hydrogen position, OH dipole orientation, and the symmetry of the crystal structure of topaz-OH. The compressional wave velocity, for both monoclinic and orthorhombic topaz-OH is greater than that of diaspore, with the following relation- $V_P^{dia} < V_P^{mon-topOH} < V_P^{orth-topOH}$ (Table 6, Fig. 9). However, for the shear wave velocity, for both monoclinic and orthorhombic topaz-OH is less than that of diaspore, with the following relation- $V_S^{dia} > V_P^{orth-topOH} > V_P^{mon-topOH}$ (Table 6, Fig. 9). The transformation of a mineral assemblage consisting of diaspore (AlOOH) and coesite (SiO_2) into topaz-OH ($Al_2SiO_4(OH)_2$) is likely to enhance density (~6%), compressional (5.5%) and shear wave velocity (1.7%). However, the enhancement of these seismic properties may be overestimated since the physical properties of an intermediate phase Pi remain unknown and is likely to be denser and seismically faster than a mixture of diaspore (AlOOH) and coesite (SiO_2). The effect of temperature also remains unknown and hence might affect our current estimates. For the hydrated subducted sedimentary layer in a subducted slab, beyond 12 GPa, topaz-OH is likely to transform to phase Egg (Ono, 1998). Recent high-pressure experiments beyond 14 GPa have revealed a new high-pressure phase topaz-OH II (Kanzaki, 2010). The proton position for this newly predicted structure remains unknown and needs to be determined. Moreover, the relative thermodynamic stability of phase Egg (the breakdown product of topaz-OH at 12 GPa) vs. topaz-OH II (stable at 14 GPa) remains unknown and needs to be determined. Given, these uncertainties, further studies are required to constrain the changes in the density, primary, and shear wave velocity associated with the mineral transformations in ASH system. It is also important to gain insight into the preferred orientation of these hydrous aluminosilicate phases at these conditions to gain a better insight into how the seismic anisotropy would evolve as a function of depth.

Acknowledgements

We thank the editor and the two anonymous reviewers for their constructive comments. MM is supported by the US National Science Foundation grant (EAR-1250477, 1520726). JT thanks Grants-In-Aid for Scientific Research (No. 26400516) from the Japan Society for the Promotion of Science.

Appendix A. Supplementary data

Supplementary data associated with this article can be found, in the online version, at http://dx.doi.org/10.1016/j.pepi.2015.11.006.

References

Birch, F., 1978. Finite strain isotherm and velocities for single crystal and polycrystalline NaCl at high-pressures and 300 K. J. Geophys. Res. 83, 1257–1268.
Bradbury, S.E., Williams, Q., 2003. Contrasting bonding behavior of two hydroxyl-bearing metamorphic minerals under pressure: clinozoisite and topaz. Am. Mineral. 88, 1460–1470.
Chantel, J., Mookherjee, M., Frost, D.J., 2012. The elasticity of lawsonite at high pressure and the origin of the low velocity layers in subduction zones. Earth Planet. Sci. Lett. 349–350, 116–125.
Chen, J., Lager, G.A., Kunz, M., Hansen, T.C., Ulmer, P., 2005. A Rietveld refinement using neutron powder diffraction data of a fully deuterated topaz, $Al_2SiO_4(OD)_2$. Acta Crystallogr. E61, i253–i255.
Chheda, T.D., Mookherjee, M., Mainprice, D., dos Santos, A.M., Molaison, J.J., Chantel, J., Manthilake, G., Bassett, W.A., 2014. Structure and elasticity of phlogopite under compression: geophysical implications. Phys. Earth Planet. Int. 233, 1–12. http://dx.doi.org/10.1016/j.pepi.2014.05.004.
Churakov, S.V., Wunder, B., 2004. Ab-initio calculations of the proton location in topaz-OH, $Al_2SiO_4(OH)_2$. Phys. Chem. Mineral. 31, 131–141.
Davies, G.F., 1974. Effective elastic-moduli under hydrostatic stress. 1. Quasi-harmonic theory. J. Phys. Chem. Solids 35, 1513–1520.
Gatta, G.D., Nestola, F., Boffa-Ballaran, T., 2006. Elastic behavior and structural evolution of topaz at high pressure. Phys. Chem. Mineral. 33, 235–242.
Gatta, G.D., Morgenworth, W., Dera, P., Petitgirard, S., Liermann, H.-P., 2014. Elastic behavior and pressure-induced structure evolution of topaz up to 45 GPa. Phys. Chem. Mineral. 41, 569–577.
Grevel, K.-D., Fasshauer, D.W., Rohling, S., 2000. Bulk moduli and *P-V-T* data of the high-pressure phases topaz-OH, $Al_2SiO_4(OH)_2$, and phase Pi, $Al_3Si_2O_7(OH)_3$. J. Conf. Abstracts 5 (1), EMPG VIII, http://www.the-conference.com/JConfAbs/5/44.html.
Grimme, S., 2006. Semiempirical GGA-type density functional constructed with a long-range dispersion correction. J. Comp. Chem. 27, 1787.
Hacker, B.R., 2008. H_2O beyond arcs. Geochem. Geophys. Geosys. 9, Q03001.
Haussühl, S., 1993. Thermoelastic properties of beryl, topaz, diaspora, sanidine and periclase. Zeit. Kristallogr. 204, 67–76.
Hohenberg, P., Kohn, W., 1964. Inhomogeneous electron gas. Phys. Rev. B. 136, B864–B871.
Jiang, F., Majzlan, J., Speziale, S., He, D., Duffy, T.S., 2008. Single-crystal elasticity of diaspore, AlOOH, to 12 GPa by Brillouin scattering. Phys. Earth. Planet. Int. 170, 221–228.
Kanzaki, M., 2010. Crystal structure of a new high-pressure polymorph of topaz-OH. Am. Mineral. 95, 1349–1352.
Karki, B.B., Stixrude, L., Wentzcovitch, R.M., 2001. High-pressure elastic properties of major materials of Earth's mantle from first principles. Rev. Geophys. 39, 507–534.
Katahara, K.W., 1996. Clay mineral elastic properties. SEG Ann. Meet. Expanded abs., 1691–1694 http://dx.doi.org/10.1190/1.1826454.
Kohn, W., Sham, L.J., 1965. Self-consistent equations including exchange and correlation effects. Phys. Rev. 140, A1133–A1138.
Komatsu, K., Kuribayashi, T., Kudoh, Y., 2003. Effect of temperature and pressure on the crystal structure of topaz, Al2SiO4(OH, F)2. J. Min. Pet. Sci. 98, 167–180.
Komatsu, K., Kagi, H., Marshall, W.G., Kuribayashi, T., Parise, J.B., Kudoh, Y., 2008. Pressure dependence of the hydrogen-bond geometry in topaz-OD from neutron powder diffraction. Am. Mineral. 93, 217–227.
Kresse, G., Furthmüller, J., 1996a. Efficiency of ab-initio total energy calculations for metals and semiconductors. Comput. Mat. Sci. 6, 15–50.
Kresse, G., Furthmüller, J., 1996b. Efficient iterative schemes for ab initio total-energy calculations using plane-wave basis set. Phys. Rev. B 54, 11169–11186.
Kresse, G., Hafner, J., 1993. Ab initio molecular-dynamics for liquid-metals. Phys. Rev. B 47, 558–561.
Kresse, G., Joubert, D., 1999. From ultrasoft pseudopotentials to the projector augmented-wave method. Phys. Rev. B 59, 1758–1775.
Mainprice, D., 1990. An efficient FORTRAN program to calculate seismic anisotropy from the lattice preferred orientation of minerals. Comput. Gesosci. 16, 385–393.
Militzer, B., Wenk, H.-R., Stackhouse, S., Stixrude, L., 2011. First-principles calculation of the elastic moduli of sheet silicates and their application to shale anisotropy. Am. Mineral. 96, 125–137.
Miller, C.F., 1985. Are strongly peraluminous magmas derived from politic sedimentary sources? J. Geol. 93, 673–689.
Monkhorst, H.J., Pack, J.D., 1976. Special points for Brillouin-zone integrations. Phys. Rev. B 13, 5188–5192.
Mookherjee, M., Speziale, S., Marquardt, H., Jahn, S., Wunder, B., Koch-Müller, M., Liermann, H.-P., 2015. Equation of state and elasticity of the 3.65 Å phase-implications for the X-discontinuity. Am. Mineral. 100, 2199–2208.
Mookherjee, M., Stixrude, L., 2006. High-pressure proton disorder in brucite. Am. Mineral. 91, 127–134.
Mookherjee, M., Stixrude, L., 2009. Structure and elasticity of serpentine at high-pressure. Earth Planet. Sci. Lett. 279, 11–19.
Mookherjee, M., Capitani, G.C., 2011. Trench parallel anisotropy and large delay times: Elasticity and anisotropy of antigorite at high pressures. Geophys. Res. Lett. 38, L09315. http://dx.doi.org/10.1029/2011GL047160.
Mookherjee, M., Bezacier, L., 2012. The low-velocity layer in subduction zone: structure and elasticity of glaucophane at high pressures. Phys. Earth Planet. Int. 208–209, 50–58.
Mookherjee, M., Mainprice, D., 2014. Unusually large shear wave anisotropy for chlorite in subduction zone settings. Geophys. Res. Lett. 41. http://dx.doi.org/10.1002/2014GL059334.
Mookherjee, M., Tsuchiya, J., 2015a. Elasticity of superhysrous phase, B, $Mg_{10}Si_3O_{14}(OH)_4$. Phys. Earth Planet. Int. 238, 42–50.
Mookherjee, M., Tsuchiya, J., 2015b. Crystal structure, equation of state, and elasticity of phase H ($MgSiO_4H_2$) at Earth's lower mantle pressures. Sci. Rep. 5, 15534. http://dx.doi.org/10.1038/srep15534.
Northrup, P.A., Leinenweber, K., Parise, J.B., 1994. The location of H in the high-pressure synthetic $Al_2SiO_4(OH)_2$ topaz analogue. Am. Mineral. 79, 401–404.
Nye, J.F., 1985. Physical Properties of Crystals. Oxford University Press, Clarendon.
Ohno, I., Yamamoto, S., Anderson, O.L., Noda, J., 1986. Determination of elastic constants of trigonal crystals by the rectangular parallelepiped resonance method. J. Phys. Chem. Solids. 47, 1103–1108.
Ohno, I., Harada, K., Yoshitomi, C., 2006. Temperature variation of elastic constants of quartz across $\alpha-\beta$ transition. Phys. Chem. Mineral. 33, 1–9.
Ono, S., 1998. Stability limits of hydrous minerals in sediment and mid-ocean ridge basalt compositions: Implications for water transport in subduction zones. J. Geophys. Res. 103, 18253–18267.
Pauling, L., 1928. The crystal structure of topaz. Proc. Nat. Acad. Sci. 14, 603–606.
Peacock, S.M., 1990. Fluid processes in subduction zones. Science 248, 329–337.
Perdew, J.P., Wang, Y., 1986. Accurate and simple density functional for the electronic exchange energy: generalized gradient approximation. Phys. Rev. B 33, 8800–8802.

Perdew, J.P., Chevary, J.A., Vosko, S.H., Jackson, K.A., Pederson, M.R., Singh, D.J., Fiolhais, C., 1991. Atoms, molecules, solids, and surfaces: applications of the generalized gradient approximation for exchange and correlation. Phys. Rev. B 46, 6671–6687.
Perdew, J.P., Burke, K., Erzerhof, M., 1996. Generalized gradient approximation made simple. Phys. Rev. Lett. 77, 3865–3868.
Ranero, C.R., Phipps Morgan, J., McIntosh, K., Reichert, C., 2003. Bending-related faulting and mantle serpentinization at the middle America trench. Nature 425, 367–373.
Ribbe, P.H., Gibbs, G.V., 1971. The crystal structure of topaz and its relation to physical properties. Am. Mineral. 56, 24–30.
Schreyer, W., 1995. Ultradeep metamorphic rocks: the retrospective viewpoint. J. Geophys. Res. 100, 8353–8366.
Stackhouse, S., Coveney, P.V., Benoit, D.M., 2004. Density functional theory based study of the dehydroxylation behavior of aluminous dioctahedral 2:1 layer type clay minerals. J. Phys. Chem. B 108, 9685–9694.
Stern, R.J., 2002. Subduction zones. Rev. Geophys. 40, 3-1–3-38.
Tsuchiya, J., Tsuchiya, T., Wentzcovitch, R.M., 2008. Vibrational properties of δ-AlOOH under pressure. Am. Mineral. 93, 477–482.
Tsuchiya, J., Tsuchiya, T., 2009. Elastic properties of δ-AlOOH under pressure- first principle investigation. Phys. Earth Planet. Int. 174, 122–127.
Tsuchiya, J., 2013a. First principles prediction of a new high pressure phase of dense hydrous magnesium silicates in the lower mantle. Geophys. Res. Lett. 40, 4570–4573.
Tsuchiya, J., 2013b. A first principles calculation of elastic and vibrational anomalies of lizardite under pressure. Am. Mineral. 98, 2046–2052.
Tulk, C.A., Gagnon, R.E., Kiefte, H., Clouter, M.J., 1994. Elastic constants of ice III by Brillouin spectroscopy. J. Chem Phys. 101, 2350.
Vaughan, M.T., Weidner, D.J., 1978. The relationship of elasticity and crystal structure in andalusite and sillimanite. Phy. Chem. Mineral. 3, 133–144.
Watenphul, A., Wunder, B., 2010. Temperature dependence of the OH-stretching frequencies in topaz-OH. Phys. Chem. Mineral. 37, 65–72.
Weaver, J.S., 1976. Application of finite strain theory to non-cubic crystals. J. Phys. Chem. Solids 37, 711–718.
Weidner, D.J., Carleton, H.R., 1977. Elasticity of coesite. J. Geophys. Res. 82, 1334–1346.
Wentzcovitch, R.M., Stixrude, L., 1997. Crystal chemistry of forsterite: a first-principle study. Am. Mineral. 82, 663–671.
Winkler, B., Hytha, M., Warren, M.C., Milman, V., Gale, J.D., Schreuer, J., 2001. Calculation of the elastic constants of the Al2SiO5 polymorphs andalusite, silimanite and kyanite. Z. Kristallogr. 216, 67–70.
Wirth, R., Vollmer, C., Brenker, F., Matsyuk, S., Kaminsky, F., 2007. Inclusions of nanocrystalline hydrous aluminium silicate "Phase Egg" in superdeep diamonds from Juina (Mato Grosso State, Brazil). Earth Planet. Sci. Lett. 259, 384–399.
Wunder, B., Rubie, D.C., RossII, C.R., Medenbach, O., Seifert, F., Schreyer, W., 1993a. Synthesis, stability, and properties of $Al_2SiO_4(OH)_2$: A fully hydrated analogue of topaz. Am. Mineral. 78, 285–297.
Wunder, B., Medenbach, O., Krause, W., Schreyer, W., 1993b. Synthesis, properties and stability of Al3Si2O7(OH)3 (phase Pi), a hydrous high-pressure phase in the system Al2O3-SiO2-H2O (ASH). Eur. J. Mineral. 5, 637–649.
Wunder, B., Andrut, M., Wirth, R., 1999. High-pressure synthesis and proper-ties of OH-rich topaz. Eur. J. Mineral. 11, 803–813.